AN EXPERIMENTAL TESTBED FOR MULTI-ROBOT TRACKING OF MANIFOLDS AND COHERENT STRUCTURES IN FLOWS

Matthew Michini, Kenneth Mallory,
Dennis Larkin, M. Ani Hsieh*
Scalable Autonomous Systems Laboratory
Mechanical Engineering and Mechanics Department
Drexel University,
Philadelphia, Pennsylvania 19104

Eric Forgoston, Philip A. Yecko†
Department of Mathematical Sciences
Montclair State University
Montclair, New Jersey 07043

ABSTRACT

In this paper, we describe the development of an experimental testbed capable of producing controllable ocean-like flows in a laboratory setting. The objective is to develop a testbed to evaluate multi-robot strategies for tracking manifolds and Lagrangian coherent structures (LCS) in the ocean. Recent theoretical results have shown that LCS coincide with minimum energy and minimum time optimal paths for autonomous vehicles in the ocean. Furthermore, knowledge of these structures enables the prediction and estimation of the underlying fluid dynamics. The testbed is a scaled flow tank capable of generating complex and controlled quasi-2D flow fields that exhibit wind-driven double-gyre flows. Particle image velocimetry (PIV) is used to extract the 2D surface velocities and the data is then processed to verify the existence of manifolds and Lagrangian coherent structures in the flow. The velocity data is then used to evaluate our previously proposed multi-robot LCS tracking strategy in simulation.

INTRODUCTION

Recent years have seen the use of autonomous underwater and surface vehicles (AUVs and ASVs) for persistent surveillance of the ocean to study the dynamics of various biological and physical phenomena, such as plankton assemblages [1], temperature and salinity profiles [2–4], and the onset of harmful algae blooms [5–7]. These studies have mostly focused on the deployment of single, or small numbers of, AUVs working in conjunction with a few stationary sensors and ASVs. While data collection strategies in these works are driven by the dynamics of the processes they study, few existing approaches explicitly account for the surrounding fluid dynamics [8, 9]. In fact, most existing works treat the effect of the surrounding fluid as external disturbances [7, 10], largely because of our limited understanding of the complexities of ocean dynamics. This is further exacerbated since existing data sets that describe oceanic flows are often finite-time and of low resolution, which limits our ability to estimate and predict their dynamics. Recently, new tools have been developed in order to study ocean transport. One of these involves determining the location of coherent structures and studying how these structures control transport.

To this end, we are interested in developing collaborative control strategies for AUVs and ASVs to track the manifolds and coherent structures on flows [11]. In realistic ocean flows, these time-dependent coherent structures, or Lagrangian coherent structures (LCS), are analogous to separatrices that divide the flow into dynamically distinct regions. LCS are extensions of stable and unstable manifolds to general time-dependent flows [12], and they carry global information about the dynamics of the flows. For two-dimensional (2D) flows, LCS are analogous to ridges defined by local maximum instability, and are quantified by local measures of finite-time Lyapunov exponents (FTLE) [13]. Recently, LCS have been shown to coincide with optimal trajectories in the ocean which minimize the energy and the time needed to traverse from one point to another [14, 15]. Since LCS denote boundaries in the flow field between dynamically distinct regions, knowledge of the LCS locations can also aid the estimation and prediction of the fluid dynamics to improve AUV and ASV navigation strategies. Furthermore, given that LCS are inherently unstable and denote regions of the flow where more escape events may occur [16], knowing LCS loca-

*{mam637, km374, djl84, mhsieh1}@drexel.edu
†{eric.forgoston,philip.yecko}@montclair.edu

tions will aid in maintaining sensors in desired monitoring regions.

Motivated by these recent developments, we previously proposed a collaborative robotic control strategy for tracking stable and unstable manifolds in 2D flows [11]. The technique relies on robots performing local measurements of the flow field and fusing this information to collaboratively track these boundaries. The collaborative control strategy was implemented using a team of three robots to track manifolds and coherent structures in static flows as well as a time-dependent model of a wind-driven double-gyre often seen in the ocean. A significant challenge in working with AUVs and ASVs for ocean monitoring applications is that field experiments are logistically difficult and costly to conduct. While validation of the robotic strategies using ocean data provided by the Naval Coastal Ocean Model (NCOM) database is a viable alternative, these data sets often have low spatio-temporal resolution. Furthermore, ocean surface current measurements in these models are often kilometers apart, limiting the usefulness of simulation results for understanding the challenges of controlling and coordinating AUVs/ASVs that are at most a few meters in size.

In this work, we describe the development of an experimental testbed capable of producing controllable ocean-like flows in a laboratory setting. The objective is to develop an experimental system that can produce high resolution and realistic quasi-2D flow fields that can be used to evaluate the performance of existing multi-robot manifold and coherent structure tracking strategies. The experimental testbed consists of a 60 cm square tank capable of generating complex and controlled flow fields that exhibit wind-driven double-gyre flow solutions. Complementing this testbed tank, we have also designed a smaller low Reynolds number apparatus (8 cm square) in which multiple gyre and jet flows can be generated, controlled, and sampled with a high degree of precision. Particle image velocimetry (PIV) is used to extract the 2D surface velocity fields and the data is then processed. We compare the experimental surface flow data with the comparable 2D analytical wind-driven double gyre model and identify and verify the existence of manifolds and coherent structures in the flow. We then use the actual flow field data to evaluate the feasibility of the collaborative tracking strategy described in [11].

The paper is structured as follows: Section 1 describes the multi-robot tracking strategy and its motivation. The development of the experimental low Reynolds number tank and the testbed tank is presented in Sec. 2, while the testbed validation can be found in Sec. 3. The computation of the FTLE is presented in Sec. 4, and Sec. 5 presents our multi-robot tracking simulation results. Lastly, future work is contained in Sec. 6.

1 MULTI-ROBOT TRACKING OF MANIFOLDS AND LCS

Ocean dynamics is of great industrial, military, and scientific interest, and the problem of predicting physical quantities or flow features is a critical one. AUVs and ASVs have filled an important gap by allowing direct and continuous monitoring, but monitoring networks are sparse, and a placement strategy is needed to optimize the impact of collected data. Such strategies cannot be formulated *a priori* due to the complexity of typical ocean circulation patterns, which are intrinsically time-dependent and three dimensional. Instead, autonomous vehicles must be able to extract important flow features and adaptively form a placement strategy that is optimal in terms of both information input and energy expenditure. To achieve this goal, individual robots must track flow and transport features that can be identified from measurements and understood using dynamical systems and fluid dynamical models.

Even within simplified models of oceanographic flows, however, features that control transport, including jets and gyres, are inherently complicated and unsteady. We therefore adopt a perturbative approach to the characterization of flow and transport features by, for example, examining the effect of periodically or stochastically forced multiple gyre flows.

The purpose of our experimental testbed is to enable the validation of existing and future collaborative robotic control strategies for tracking material lines that separate regions of flow with distinct fluid dynamics. We briefly summarize our existing tracking strategy for the sake of completeness and refer the interested reader to [11] for further details.

As mentioned previously, the problem of tracking manifolds and coherent structures in complex flows is similar to tracking stable (and unstable) manifolds of a general nonlinear dynamical system where the manifolds separate regions in phase space with distinct dynamical behaviors. Our existing collaborative control strategy was developed assuming 2D conservative planar flows where the material lines correspond to the stable and unstable manifolds. The tracking strategy was inspired by the Proper Interior Maximum (PIM) Triple Procedure [17] – a numerical technique designed to find stationary trajectories in chaotic regions with no attractors. The strategy assumes a team of three robots whose objective is to maintain a saddle straddling formation across the manifold/boundary of interest. By maintaining a saddle straddling formation and leveraging the flow field dynamics, the team iteratively traces out the location of the ridge in the flow.

Given a team of three robots, we identify them as robots $\{L,C,R\}$. To successfully track the manifold of interest, denoted by B_S, robot C must remain close to B_S using only local measurements of the velocity field provided by the rest of the team. As such, robot C is the tracking robot while robots L and R are tasked to maintain the *straddle formation* across the B_S at all times. We assume the following 2D kinematic model for each of the AUVs:

$$\dot{x}_i = V_i \cos\theta_i + u_i, \tag{1a}$$

$$\dot{y}_i = V_i \sin\theta_i + v_i, \tag{1b}$$

where $\mathbf{x}_i = (x_i, y_i)^T$ denotes the vehicle's position in the plane, V_i and θ_i denote respectively the vehicle's speed and

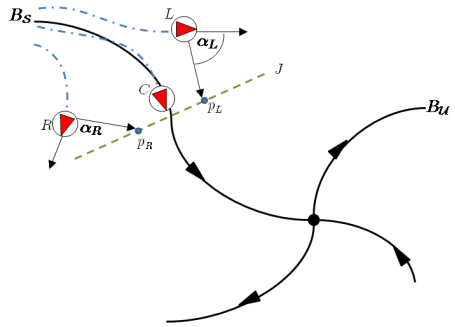

Figure 1. THREE ROBOTS TRACKING B_S IN A GIVEN CONSERVATIVE VECTOR FIELD. THE BLUE DASH-DOT LINES REPRESENT THE INDIVIDUAL ROBOT TRAJECTORIES, THE GREEN DASHED LINE REPRESENTS THE SADDLE STRADDLE LINE SEGMENT J, AND $\mathbf{P}_L$ AND $\mathbf{P}_R$ DENOTE THE TARGET POSITIONS FOR ROBOTS L AND R, RESPECTIVELY, WHEN EXECUTING U_A.

heading, and $\mathbf{u}_i = (u_i, v_i)^T$ denotes the fluid velocity experienced/measured by the i^{th} vehicle. Here V_i and θ_i are the control inputs for each vehicle.

The controller for the straddling robots consists of two discrete states: a passive control state, U_P, and an active control state, U_A. The robots initialize in the passive state U_P where the objective is to follow the flow of the ambient vector field. Therefore, $V_i = 0$ for $i = L, R$. Robots execute U_P until they reach a maximum allowable separation distance from the tracking robot C. When robots L and R are too far from robot C, they switch to the active control state, U_A, where the objective is to navigate to a point on the next saddle straddle line segment. A sketch of the collaborative control strategy is shown in Fig. 1.

As the robots maintain the formation, they constantly sample the velocity of the surrounding flow field and communicate these measurements and their relative positions to robot C. The tracking robot C uses the velocity measurements provided by robots L and R to interpolate the vector field along a collection of points located on the saddle straddling line segment, denoted by J in Fig. 1, given by robots L and R's position. Then robot C's estimate of the manifold is given by the point on J with either the maximum or minimum velocity depending on whether the team is tracking the unstable or stable manifold. In this work, we assume full communication capability among the robots. In other words, we assume that each robot can know the positions of the other robots in relation to itself and that robot C can communicate information about the projected saddle straddle line segment to robots L and R. By employing this technique iteratively, the team can estimate and track the location of the manifold.

It is important to note that Lagrangian coherent structures are time-dependent extensions of the stable and unstable manifolds of time-independent systems. In 2D flows, LCS are essentially the ridges/boundaries defined by local maximum instability, and quantified by local measures of Finite-Time Lyapunov Exponents (FTLE) [13]. To validate and evaluate existing and future collaborative robotic control strategies for tracking manifolds and coherent structures in complex flows that meet the various requirements described previously, we have designed an experimental testbed.

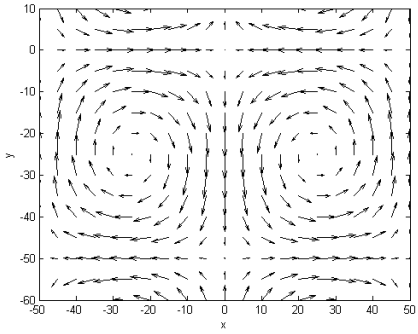

Figure 2. VECTOR FIELD OF THE MODEL GIVEN BY (2) FOR TWO GYRES WITH $A = 10$, $\mu = 0.005$, $\varepsilon = 0$, $\psi = 0$, $I = 0.01$, AND $S = 50$.

2 EXPERIMENTAL TESTBED

In this section, we describe the development of our experimental flow tank built to generate controllable flow fields that exhibit the transport-controlling features relevant to robot placement. Since realistic quasi-geostrophic ocean models exhibit double-gyre flow solutions, our objective is to develop a laboratory testbed capable of generating flows that can be described by the wind-driven double-gyre flow model given by:

$$\dot{x} = -\pi A \sin(\pi \frac{f(x,t)}{s}) \cos(\pi \frac{y}{s}) - \mu x + \eta_1(t), \tag{2a}$$

$$\dot{y} = \pi A \cos(\pi \frac{f(x,t)}{s}) \sin(\pi \frac{y}{s}) \frac{df}{dx} - \mu y + \eta_2(t), \tag{2b}$$

$$\dot{z} = 0, \tag{2c}$$

$$f(x,t) = \varepsilon \sin(\omega t + \psi) x^2 + (1 - 2\varepsilon \sin(\omega t + \psi)) x. \tag{2d}$$

When $\varepsilon = 0$, the multi-gyre flow is time-independent, while for $\varepsilon \neq 0$, the gyres undergo a periodic expansion and contraction in the x direction. In (2), A approximately determines the amplitude of the velocity vectors, $\omega/2\pi$ gives the oscillation frequency, ε determines the amplitude of the left-right motion of the separatrix between the gyres, ψ is the phase, μ determines the dissipation, s scales the dimensions of the workspace, and $\eta_i(t)$ describes a stochastic white noise with mean zero and standard deviation $\sigma = \sqrt{2I}$, for noise intensity I. Fig. 2 shows the vector field of a two-gyre model.

2.1 Low Reynolds number tank

In order to impose precisely formed perturbations onto controlled and realistic flows, we have designed laboratory experiments in the low Reynolds number regime. An 8 cm square transparent tank is filled to a depth $d = 2$ cm with a glycerol-water mix and driven by a 4 x 4 lattice of submerged disks mounted to an array of shafts linked by gears. The apparatus

is designed so that the two adjacent 4 x 2 sets of disks have separate stepper motors, controllers and gears, such that they may be independently driven at any time-dependent angular velocity function from a simple MATLAB code. High quality PIV is obtained using laser light sheet illuminated 50 μm diameter tracer particles and a high speed video camera, as seen in Fig. 3. Because the Reynolds numbers in these experiments are in the range $Re \sim O(10) - Re \sim O(1000)$, the flow is not a realistic model of ocean gyres. Nevertheless, these laboratory flows have a number of features in common with actual oceanographic flows as well as double-gyre model flows: both are quasi-two-dimensional and the gyre centers are free to wander under perturbation (Fig. 3(c)). Within this framework, we have applied a range of perturbative forcing functions in which the disk lattice is driven using time-varying and stochastic rotational velocities. We readily observe that time-dependent perturbations lead to transport across the gyre boundaries (Fig.3(a)-3(b)), as first noted by Aref [18], and break the time reversibility of the flow, as discussed recently by Eckhardt and Hascoët [19].

These low Reynolds number experiments provide a valuable template for the design of flows and control strategies in the testbed tank, described next in Sec. 2.2. First, the low Re flows are strongly 2D: a single tracer remains within the 0.6 mm thick laser sheet for 20 or more orbits. Moreover, the flowfield may be captured at any depth, allowing us to quantify the role of weak three-dimensionality. Because of its small size, ideal PIV conditions are maintained and, as needed, particle tracking velocimetry (PTV) may be simultaneously performed on a small number of larger particles that emulate AUVs/ASVs. Finally, the operating regime of the low Reynolds number tank may be extended using glycerine-water mixtures to $O(10^3)$ or more, overlapping the regime of the testbed tank.

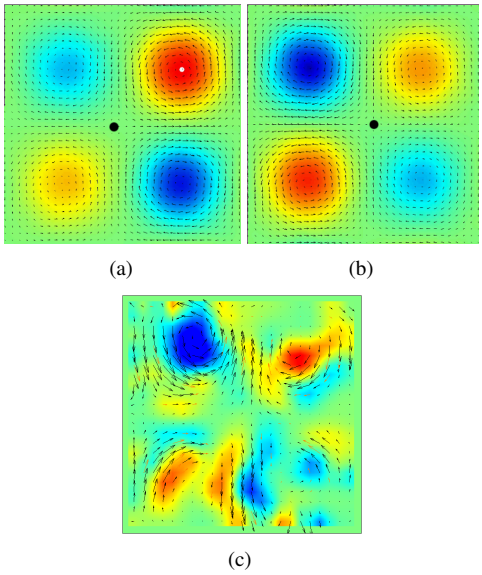

Figure 3. PIV FLOWFIELDS (A-B) SHOWING CONTROLLED SHIFT OF CENTRAL SEPARATRIX DUE TO TEMPORAL VARIABILITY IN THE RELATIVE VELOCITIES OF THE LEFT AND RIGHT GYRE PAIRS; (C) A 30-70 VOLUME MIX OF GLYCEROL-WATER SHOWING THE UNSTEADY GYRES AT RE ≈ 1000.

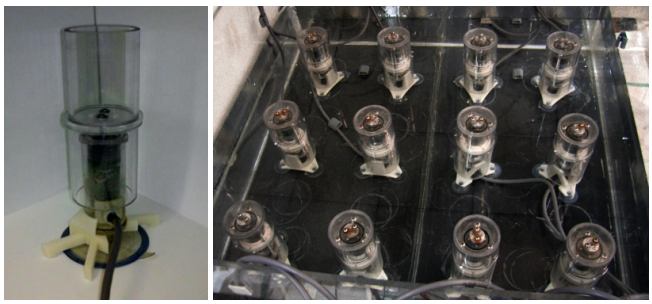

Figure 4. (A) FLOW TANK CYLINDRICAL POSTS ATTACHED TO MOTOR. (B) $60 \times 60 \times 30\, CM^3$ EXPERIMENTAL FLOW TANK.

2.2 Testbed Tank

While the low Reynolds number tank is useful in precisely measuring flow-dependent transport features, it is of limited use when considering the interaction of AUVs and ASVs with transport. To create a more realistic experimental platform where multiple robots may track features in complex time-dependent flows in which they are immersed, we require a larger flow field in which more unsteady, higher Reynolds number flows can be generated, still with some degree of control over perturbations. At Reynolds numbers in the range Re $> O(10^4)$, sheared flows such as multiple gyres will exhibit strongly nonlinear response to driving and display complex, time-dependent flow patterns. Nevertheless, we must be able to control the coarse features of the flows, such as the mean sizes and locations of the gyres and their boundaries – in other words, the transport controlling features. Ultimately, our laboratory experiment must also accommodate the deployment of a small network of robots within the flow. The dominant flow features must therefore remain large enough in scale that the trajectory of a robot within the flow is approximately that of a tracer.

To achieve this, we built a $60 \times 60 \times 30$ cm^3 acrylic flow tank. The flow field is generated using 12 DC geared motors each mounted to an acrylic cylinder that is approximately 6 *cm* in diameter and 14 cm in height (see Fig. 4(a)). The motors are equipped with magnetic encoders to enable closed-loop control of the motor speeds. Each motorized cylinder is then mounted perpendicular to the bottom of the tank via suction cups and stabilizing plastic bases as shown in Fig. 4(b).

To generate the flow field, the tank was filled with water to a depth of 14 cm. The dynamics of the flow field can be changed by setting the speed and direction of the motorized cylinders. A time-independent flow field was created by placing the 12 motorized cylinders on a 4×3 grid. The grid of cylinders were set to rotate at the same constant speed but each in an opposing direction. In other words, each motor rotated in a direction opposite to the ones adjacent to it on the grid. Time-varying flow fields can be generated by periodically changing the direction and the

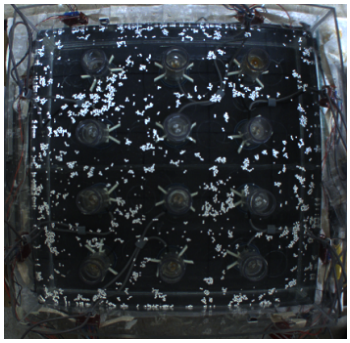

(a)

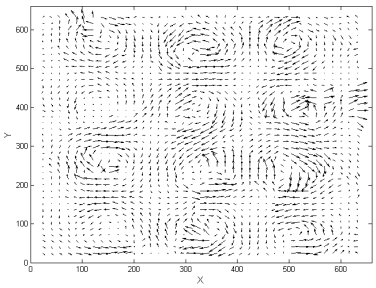

(b)

Figure 5. (A) EXPERIMENTAL SETUP OF FLOW TANK WITH 12 DRIVEN CYLINDERS. (B) FLOW FIELD FOR IMAGE (A) OBTAINED VIA PARTICLE IMAGE VELOCIMETRY (PIV).

speed of specific cylinders in the grid. In this work, we focus on creating time-independent flow fields.

Particle image velocimetry (PIV) is used to track the surface flow field [20]. In our testbed, we employ a color camera and circular paper markers 0.3 cm in diameter. The raw images were then processed using the open-source MATLAB PIV Toolbox [21] to extract the surface velocities of the fluid. A sample frame of the experimental setup is shown in Fig. 5(a) and the extracted velocity field is shown in Fig. 5(b). In recent tests, we have supplanted the paper markers with water-resistant polypropylene spheres, which are more homogeneous and are less prone to clumping behavior. We are also experimenting with a surfactant to reduce surface tension, which will reduce particle clumping.

3 TESTBED VALIDATION

The analytical basis for our tank is the static wind-driven double-gyre model given by (2). To achieve a similar 2D flow pattern, the motors are placed at fixed positions in the tank. We used two methods to compare the experimental data with the analytical double-gyre model. First, Fourier analysis tools were used in order to identify the dominant frequencies in the flow field for both the analytical model and the experimental data. We then used a Dynamic Mode Decomposition (DMD) to compare the dominant dynamic modes of the model and the experimental data.

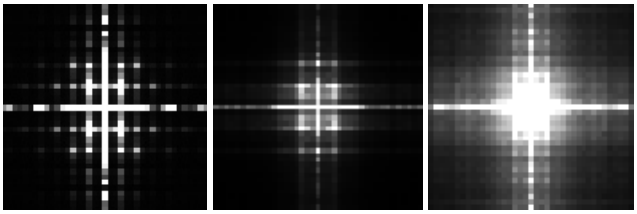

(a) Wind-Driven Double-Gyre (b) Mean Data (c) Snapshot of Data

Figure 6. FAST FOURIER TRANSFORM OF VELOCITY MAGNITUDES OF A) THE WIND-DRIVEN DOUBLE-GYRE MODEL, B) THE MEAN OF THE EXPERIMENTAL DATA AND C) A SINGLE TIME FRAME OF THE EXPERIMENTAL DATA. THESE IMAGES HAVE BEEN SHIFTED SUCH THAT THE ZERO FREQUENCY LOCATIONS ARE AT THE CENTER OF THE IMAGE.

3.1 Fourier Analysis

Figure 6 presents the Fast Fourier Transforms (FFT) of velocity magnitudes for both the double-gyre model and experimental data. The figure shows that the experimental data (Figs. 6(b) and 6(c)) and the analytical model (Fig. 6(a)) exhibit similar frequency components, despite the high levels of noise present in the experimental data. Noise in the experimental data can be seen by comparing Fig. 6(b), which represents a time average of the experimental data, with Fig. 6(c), which is an unfiltered snapshot of the data.

The off-axis vertical lines are symmetric about the x-axis and represent the frequency (and corresponding harmonics) at which the flow changes direction in the y-direction. Similarly, the off-axis horizontal lines are symmetric about the y-axis and represent the frequency (and corresponding harmonics) across the x-direction. It should be noted that the horizontal lines are farther from the origin than the vertical ones. This tells us that the flow changes direction faster in the y-direction. This effect is associated with the fact that the motors are arranged in a 4×3 grid with columns of 4 motors placed along the y-direction.

3.2 Dynamic Mode Decomposition

In addition to the FFT analysis, we compared the experimental data with the analytical model using the Dynamic Mode Decomposition (DMD) technique [22, 23]. In general, the DMD approach described in [22] yields a total of $k-1$ dynamic modes where k denotes the total number of measurements, or frames, obtained at each sampling period. While the approach enables accurate reconstruction of the original flow field, it does not easily distinguish between dominant and non-dominant dynamic modes, i.e. dominant flow dynamics and noise. Therefore, we employ the optimized DMD technique presented in [23].

The main advantage of the optimized DMD approach is that it also allows the user to select the number of dominant modes used to provide a reduced order representation the flow field. Since it is difficult to determine the minimum number of modes for a given experimental data set, we performed the decomposition assuming varying numbers of modes and compared the

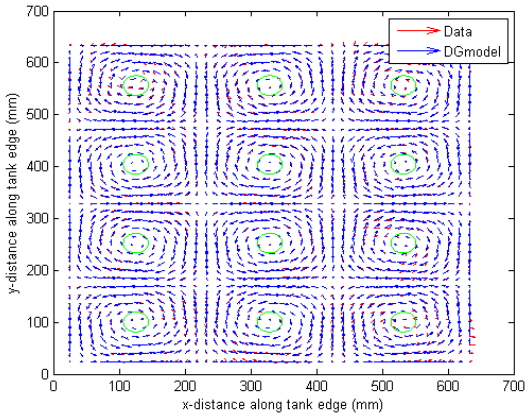

Figure 7. OVERLAYED VECTOR FIELDS FROM THE DOMINANT MODE OF THE DOUBLE-GYRE MODEL AND THE EXPERIMENTAL DATA. GREEN CIRCLES DENOTE THE LOCATIONS OF THE MOTORS.

error, percentage of energy captured in the dominant modes, and the total number of iterations. We found that after 2-6 iterations, the residuals in the weights associated with the principal modes converge to a minimum value. Using 2 principal modes required more iterations to converge, while using 5 or more principal modes resulted in a very fast convergence with the lowest error. Since the solutions for 2-6 principal modes all yielded roughly the same minimum residual, we considered solutions that contained the majority of the energy in a single mode. By comparing the weights on each principal mode for each solution, it was determined that the 2 principal mode optimized DMD solution best captured the primary dynamics of the experimental data since it contained almost 85% of the energy of the system in the main dominant mode.

To compare the dominant flow fields obtained using the optimized DMD technique for the model given by (2) and our experimental data, we computed the errors in the magnitude and the phase of the velocity vectors at each point in the flow field. Fig. 7 shows an overlay of the extracted dominant modes of the model and the experimental data. The differences in velocity magnitude and phase are shown in Figs. 8 and 9. The largest errors arise in regions where the flow interacts with the spinning cylinders. This is not unexpected since the PIV velocity data in these regions is very noisy and does not provide any information about the flow dynamics. Taken together, Figs. 7-9 demonstrate substantial agreement between the analytical model and the experimental data.

4 COMPUTATION OF FTLE

One method that can be used to understand transport and which quantifies localized sensitive dependence to initial conditions in a given fluid flow involves the computation of finite-time Lyapunov exponents (FTLE). In a deterministic setting, the FTLE also gives an explicit measure of phase space uncertainty. Given a dynamical system, one is often interested in determining how particles that are initially infinitesimally close behave

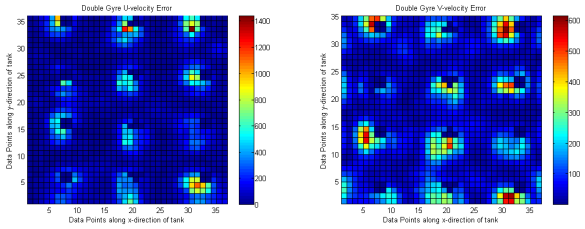

(a) Error in u-velocity (b) Error in v-velocity

Figure 8. VELOCITY ERROR IN (A) X-DIRECTION (U) AND (B) Y-DIRECTION (V). BLUE COLORS DENOTE LITTLE TO NO ERROR WHILE RED COLORS DENOTE PEAK ERROR.

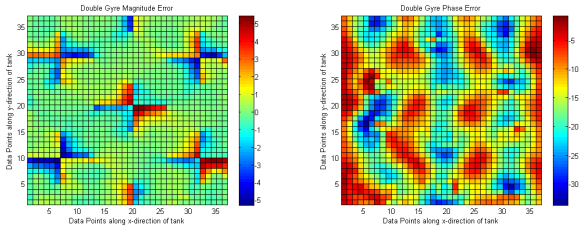

(a) Error in vector magnitude (b) Error in vector phase

Figure 9. MAGNITUDE AND PHASE ERROR. FOR MAGNITUDE ERROR BLUE REPRESENTS A REGION WITH A VELOCITY MAGNITUDE LOWER THAN PREDICTED AND RED REPRESENTS HIGHER THAN PREDICTED. PHASE ERROR WAS ALWAYS NEGATIVE, WHERE RED REPRESENTS THE LEAST ERROR AND BLUE REPRESENTS THE GREATEST ERROR.

as time $t \to \pm\infty$. It is well-known that a quantitative measure of this asymptotic behavior is provided by the classical Lyapunov exponent [24]. In a similar manner, a quantitative measure of how much nearby particles separate after a specific amount of time has elapsed is provided by the FTLE.

Although the FTLE theory can be extended to arbitrary dimension [25], here we consider a 2D velocity field $\boldsymbol{v} : \mathbb{R}^2 \times I \to \mathbb{R}^2$ which is defined over the time interval $I = [t_i, t_f] \subset \mathbb{R}$ and the following system of equations:

$$\dot{\boldsymbol{z}}(t; t_i, \boldsymbol{z}_0) = \boldsymbol{v}(\boldsymbol{z}(t; t_i, \boldsymbol{z}_0), t), \tag{3a}$$
$$\boldsymbol{z}(t_i; t_i, \boldsymbol{z}_0) = \boldsymbol{z}_0, \tag{3b}$$

where $\boldsymbol{z} = (x, y)^T \in \mathbb{R}^2$, $\boldsymbol{z}_0 \in \mathbb{R}^2$, and $t \in I$.

As previously stated, the trajectories of a dynamical system in the infinite time limit can be quantified with the system's Lyapunov exponents. If one restricts the Lyapunov exponent calculation to a finite time interval, the resulting exponents are the FTLE. In practice, the FTLE computation involves consideration of nearby initial conditions and the determination of how the trajectories associated with these initial conditions evolve in time. Therefore, the FTLE provides a local measure of sensitivity to initial conditions and measures the growth rates of the linearized dynamics about the trajectories. Since the details of the derivation of the FTLE [25–30] as well as applications that employ

the FTLE [31–33] have appeared in the literature, we shall only briefly summarize the procedure.

The solution of the dynamical system from the initial time t_i to the final time $t_i + T$ can be viewed as the flow map $\phi_{t_i}^{t_i+T}$ which is defined as follows:

$$\phi_{t_i}^{t_i+T} : \boldsymbol{z}_0 \mapsto \phi_{t_i}^{t_i+T}(\boldsymbol{z}_0) = \boldsymbol{z}(t_i + T; t_i, \boldsymbol{z}_0). \tag{4}$$

We consider an initial point located at $\boldsymbol{z}$ at $t_i = 0$ along with a perturbed point located at $\boldsymbol{z} + \delta\boldsymbol{z}(0)$ at $t_i = 0$. Using a Taylor series expansion, one finds that

$$\delta\boldsymbol{z}(T) = \frac{d\phi_{t_i}^{t_i+T}(\boldsymbol{z})}{d\boldsymbol{z}}\delta\boldsymbol{z}(0) + O(||\delta\boldsymbol{z}(0)||^2). \tag{5}$$

Dropping the higher order terms, the magnitude of the linearized perturbations is given as

$$||\delta\boldsymbol{z}(T)|| = \sqrt{\langle\delta\boldsymbol{z}(0), \Delta\delta\boldsymbol{z}(0)\rangle}, \tag{6}$$

where Δ is the right Cauchy-Green deformation tensor and is given as follows:

$$\Delta(\boldsymbol{z}, t_i, T) = \left(\frac{d\phi_{t_i}^{t_i+T}(\boldsymbol{z}(t))}{d\boldsymbol{z}(t)}\right)^* \left(\frac{d\phi_{t_i}^{t_i+T}(\boldsymbol{z}(t))}{d\boldsymbol{z}(t)}\right), \tag{7}$$

with * denoting the adjoint. Then the FTLE can be defined as

$$\sigma(\boldsymbol{z}, t_i, T) = \frac{1}{|T|}\ln\sqrt{\lambda_{\max}(\Delta)}, \tag{8}$$

where $\lambda_{\max}(\Delta)$ is the maximum eigenvalue of Δ.

For a given $\boldsymbol{z} \in \mathbb{R}^2$ at an initial time t_i, Eq. (8) gives the maximum finite-time Lyapunov exponent for some finite integration time T (forward or backward), and provides a measure of the sensitivity of a trajectory to small perturbations.

As an example, Fig. 10 shows a snapshot of the forward time FTLE field computed using the extracted PIV velocity field for one of the flow tank's experimental runs. One can see in Fig. 10 that there are ridges (in red) of locally maximal FTLE values. These ridges correspond, to a good approximation (though see Ref. [34]), to Lagrangian coherent structures, and effectively separate the phase space into distinct dynamical regions.

5 SIMULATION RESULTS

As mentioned previously, particle image velocimetry is used to extract the surface flow field of the tank. As such, surface velocity data is provided at 7.5 frames per second and for a grid of 39 by 39 points. The flow field data was then used to validate the collaborative control strategy described in Sec. 1.

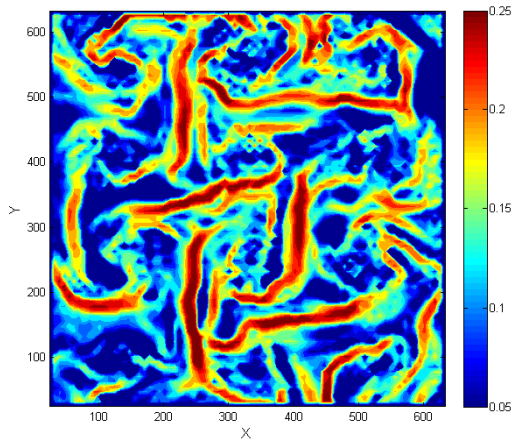

Figure 10. FORWARD FTLE FIELD COMPUTED USING THE EXTRACTED PIV VELOCITY FIELD. THE INTEGRATION TIME IS $T = 10$ WITH A GRID RESOLUTION OF 8 PIXELS IN BOTH X AND Y.

In our simulations, we employed an integration time of 0.01. Since the flow field is sparse in relation to all the possible positions of the robotic vehicles, we employ the *inverse distance weighting method* described in [35] to interpolate the flow field to obtain the velocities at positions not on the grid. For a given set of velocity measurements $\hat{\mathbf{u}}_i(t)$ and corresponding positions $\mathbf{x}_i(t)$, the velocity vector at some point $\mathbf{q}_k$ is given by

$$\mathbf{u}(\mathbf{q}_k) = \sum_j \sum_{i=1}^{N} \frac{w_{ij}\mathbf{u}_i(j)}{\sum_j \sum_{i=1}^{N} w_{ij}}$$

where $w_{ij} = \|\mathbf{x}_i(j) - \mathbf{q}_i\|^{-2}$. While there are numerous vector field interpolation techniques available [35–37], we chose the inverse distance weighting method due to its ease of implementation as well as its reliance on data that can be obtained via local sensing alone.

Figures 11(a)-(h) show the use of the control strategy described in Sec. 1 to track the material lines (or coherent structures) separating regions with distinct flow dynamics in the flow generated by our experimental tank. As mentioned previously, these lines are quantified by local measures of FTLEs. In these experiments, all the rotating cylinders were set at constant speed. As such, the material lines exhibited in the flows are approximately time-independent and stochastic. And while we do see the team occasionally traverse across regions with local maximum FTLE measures, the team quickly resumes straddling another neighboring FTLE ridge. The most likely explanation for this temporary break in the saddle straddling formation is that the team approached a local saddle point in the flow. As the team approaches the saddle point from one side, the other side of the saddle point in the flow field reverses direction. As such, the robots would be temporarily pushed away from the saddle point until they find another manifold to track. This is backed by the positions of rotating cylinders in relation to the FTLE ridges as shown in Fig. 12. We note that saddle points are located in the

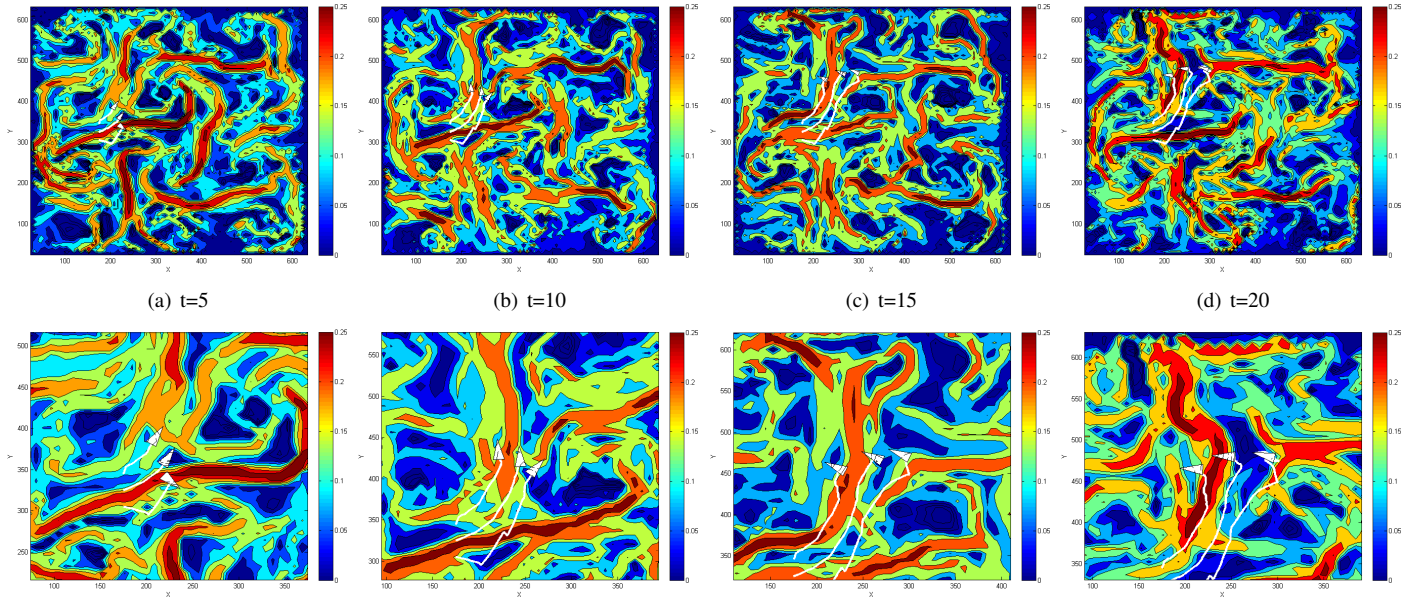

(a) t=5 (b) t=10 (c) t=15 (d) t=20

(e) t=5 (f) t=10 (g) t=15 (h) t=20

Figure 11. FORWARD FTLE FIELD OVERLAID WITH TRAJECTORIES OF THE TEAM OF 3 ROBOTS TRACKING THE MANIFOLDS/COHERENT STRUCTURES OF THE FLOW FIELD GENERATED BY OUR EXPERIMENTAL TANK. ROBOTS ARE SHOWN AS WHITE TRIANGLES AND THE TRAJECTORIES OF THE STRADDLING ROBOTS ARE SHOWN AS WHITE SOLID LINES. THE ESTIMATED LCS IS SHOWN AS A WHITE LINE, CORRESPONDING TO THE TRAJECTORY OF THE CENTER ROBOT. THE FRAMES ARE TAKEN AT $T = 5$, $T = 10$, $T = 15$ AND $T = 20$. THE BOTTOM ROW IS A SET OF ZOOMED IN VIEWS OF THE FRAMES ABOVE THEM.

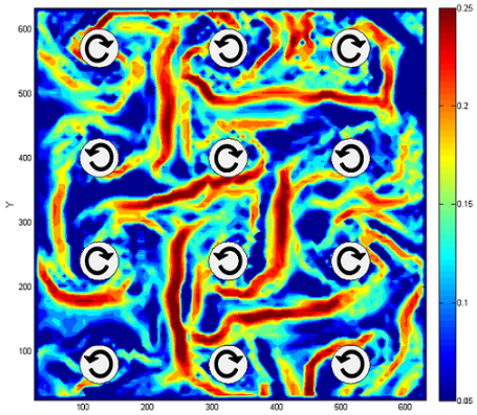

Figure 12. APPROXIMATE POSITIONS OF THE TANK CYLINDERS, AND THEIR ROTATIONAL DIRECTIONS, IN RELATION TO THE COMPUTED FLTE FIELD.

middle of every set of four rotating cylinders.

6 FUTURE WORK

We presented the development of a 60 cm square experimental testbed to enable the validation and evaluation of distributed multi-robot tracking of manifolds and coherent structures in flows. In addition, we reported on the development of a smaller scale flow tank for generating realistic flows that exhibit coherent structures that are important for quantifying transport phenomena. Furthermore, these structures play an important role in developing minimum energy and minimum time optimal paths for AUVs in the ocean. We showed how the flow fields generated with our experimental testbed exhibit coherent structures quantified by local measures of maximum FTLE and validated our existing multi-robot tracking strategies using the extracted flow field data.

An immediate direction for future work is to evaluate the soundness of our experimental testbed in the generation of controllable and repeatable realistic flow fields. Numerous experimental and computational techniques can be used to evaluate the soundness of the flow fields extracted from our system. One technique is to reverse the flow field and compare the resulting FTLE structures with those computed using the forward flow field. This can be easily achieved by reversing the rotational direction of every cylinder in the tank. A second approach is to compare the extracted flow field with a partial differential equation model of the flow field in the tank. This is one direction of significant interest.

Furthermore, precise control of the flow and its LCS features can be achieved in the low Reynolds number tank, allowing us to fine-tune our tracking strategies in a number of ways. For example, the central four gyres in this tank form a boundary-isolated “four roller mill”, when driven by rods and a four gyre model when driven by disks. A model AUV placed into this region will directly reveal the role of robot shape on its transport, as determined by its interaction with robot-scale shear and strain

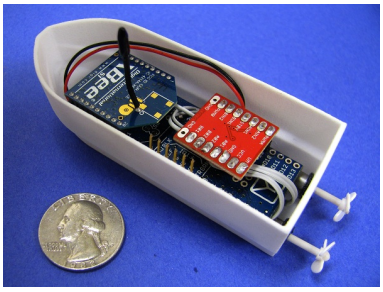

Figure 13. MICRO ASV UNDER DEVELOPMENT FOR USE IN PROTOTYPING TRACKING STRATEGIES IN THE $3M \times 3M$ TANK, WITH A US QUARTER FOR REFERENCE.

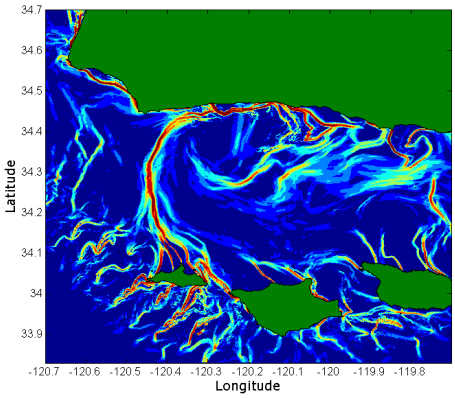

Figure 14. COHERENT STRUCTURES IN THE SANTA BARBARA CHANNEL DURING A JUNE 2012 EDDY EVENT COMPUTED USING OCEAN SURFACE CURRENT DATA PROVIDED BY THE SCRIPPS INSTITUTION OF OCEANOGRAPHY (UCSD).

signatures in the flow. This is of particular interest since our tracking strategies depend on local sampling of the flow field using a robot's onboard sensors. By understanding the interactions between the robot shape and the surrounding fluid, we can better understand their impact on the robot's ability to extract flow information from their onboard sensors.

To enable experimental validation of all tracking strategies using a multi-vehicle testbed, we have begun scaling our experimental testbed to a $3\text{m} \times 3\text{m} \times 0.5\text{m}$ flow tank. The larger tank enables the development and deployment of micro-autonomous surface vehicles to enable validation and evaluation of all tracking strategies in a controlled laboratory setting. This strategy provides an economic way to benchmark and evaluate various AUV/ASV coordination strategies in the presence of more realistic fluid dynamics. The micro-ASV under development for this task is pictured in Fig. 13. A fitting direction for future work includes the consideration of ASV and AUV dynamics in the LCS tracking strategy.

Finally, we are interested in extending our tracking strategy for use with real ocean data. The California coast is highly instrumented with high-frequency (HF) radar ocean current monitoring stations which provide high-resolution ocean current data at various locations along the coast. Since the goal of the experimental testbed is to emulate ocean flows, we have begun to apply the cooperative control strategy to areas along the coast for which there is sufficient current data. In particular, the Santa Barbara Channel is highly interesting, primarily because there is a recurring small-scale eddy (roughly 40 km in diameter) which appears between the Channel Islands and the mainland. This eddy results in an area of highly divergent flow stringing between the mainland and San Miguel Island, which can be easily seen by applying the FTLE technique on the interpolated ocean data. Figure 14 shows a snapshot of the forward-time FTLE field for the Santa Barbara Channel during a strong eddy event in June 2012.

Since this area is well-instrumented and exhibits flow features of interest to us, it provides an even larger scale simulation testbed for our tracking algorithms. If the viability of the tracking strategy can be demonstrated for this area, it can then be applied to areas for which there is not an abundance of information. We can then use the tracking strategy in simulations of realistic situations in the ocean, such as oil spills or biological events.

ACKNOWLEDGMENT

This work was supported by the Office of Naval Research (ONR) by ONR Award No: N000141211019. EF is supported by the Naval Research Laboratory (Award No. N0017310-2-C007). PAY thanks Jun Zhang, Applied Math Lab, Courant Institute, NYU, for use of the lab and hosting initial work in the low Reynolds number tank.

REFERENCES

[1] Caron, D., Stauffer, B., Moorthi, S., Singh, A., Batalin, M., Graham, E., Hansen, M., Kaiser, W., Das, J., de Menezes Pereira, A., A. Dhariwal, B. Z., Oberg, C., and Sukhatme, G., 2008. "Macro- to fine-scale spatial and temporal distributions and dynamics of phytoplankton and their environmental driving forces in a small subalpine lake in southern California, USA". *Limnol. Oceanogr.,* ***53***(5), pp. 2333–2349.

[2] Lynch, K. M., Schwartz, I. B. Yang, P., and Freeman, R. A., 2008. "Decentralized environmental modeling by mobile sensor networks". *IEEE Trans. Robotics,* ***24***(3), pp. 710–724.

[3] Wu, W., and Zhang, F., 2011. "Cooperative exploration of level surfaces of three dimensional scalar fields". *Automatica, the IFAC Journall,* ***47***(9), pp. 2044–2051.

[4] Sydney, N., and Paley, D. A., 2011. "Multi-vehicle control and optimization for spatiotemporal sampling". In IEEE Conf. Decis. Contr., pp. 5607–5612.

[5] Zhang, F., Fratantoni, D. M., Paley, D., Lund, J., and Leonard, N. E., 2007. "Control of coordinated patterns for ocean sampling". *International Journal of Control,* ***80***(7), pp. 1186–1199.

[6] Chen, V., Batalin, M., Kaiser, W., and Sukhatme, G., 2008. "Towards spatial and semantic mapping in aquatic environments". In IEEE Int. Conf. Robot. Automat., pp. 629–636.

[7] Das, J., Py, F., Maughan, T., O'Reilly, T., Messié, M., Ryan, J., Sukhatme, G., and Rajan, K., 2012. "Coordinated sampling of dynamic oceanographic features with underwater vehicles and drifters". *Int. J. Robot. Res.,* ***31***(5), pp. 626–646.

[8] Lolla, T., Ueckermann, M. P., Haley, P., and Lermusiaux, P. F. J., 2012. "Path planning in time dependent flow fields using level set methods". In Submitted to IEEE International Conference on Robotics and Automation.

[9] DeVries, L., and Paley, D. A., 2011. "Multi-vehicle control in a strong flowfield with application to hurricane sampling". *Accepted for publication in the AIAA J. Guidance, Control, and Dynamics*.

[10] Williams, R., and Sukhatme, G., 2012. "Probabilistic spatial mapping and curve tracking in distributed multi-agent systems". In Submitted to IEEE International Conference on Robotics and Automation.

[11] Hsieh, M. A., Forgoston, E., Mather, T. W., and Schwartz, I. B., 2012. "Robotic manifold tracking of coherent structures in flows". In in the Proc. of the IEEE International Conference on Robotics and Automation.

[12] Haller, G., and Yuan, G., 2000. "Lagrangian coherent structures and mixing in two-dimensional turbulence". *Phys. D,* ***147***, December, pp. 352–370.

[13] Shadden, S. C., Lekien, F., and Marsden, J. E., 2005. "Definition and properties of lagrangian coherent structures from finite-time lyapunov exponents in two-dimensional aperiodicflows". *Physica D: Nonlinear Phenomena,* ***212***(3-4), pp. 271 – 304.

[14] Inanc, T., Shadden, S., and Marsden, J., 2005. "Optimal trajectory generation in ocean flows". In American Control Conference, 2005. Proceedings of the 2005, pp. 674 – 679.

[15] Senatore, C., and Ross, S., 2008. "Fuel-efficient navigation in complex flows". In American Control Conference, 2008, pp. 1244 –1248.

[16] Forgoston, E., Billings, L., Yecko, P., and Schwartz, I. B., 2011. "Set-based corral control in stochastic dynamical systems: Making almost invariant sets more invariant". *Chaos,* ***21***(013116).

[17] Nusse, H. E., and Yorke, J. A., 1989. "A procedure for finding numerical trajectories on chaotic saddles". *Physica D Nonlinear Phenomena,* ***36***, jun, pp. 137–156.

[18] Aref, H., 1984. "Stirring by chaotic advection". *J. Fluid Mech.,* ***143***, pp. 1–21.

[19] Eckhardt, B., and Hascoët, E., 2005. "Breaking time reversal symmetry by viscous dephasing". *Phys. Rev. E,* ***72***, p. 037301.

[20] Adrian, R. J., Wildes, R. P., Amabile, M. J., marie Lanzillotto, A., and shyng Leu, T., 1991. "Particle imaging techniques for experimental fluid mechanics". In In Proc. Conf. Comp. Vision Pattern Rec, pp. 969–975.

[21] MATLAB piv toolbox. `http://www.oceanwave.jp/softwares/mpiv/`.

[22] Schmid, P. J., 2010. "Dynamic Mode Decompostion of Numerical and Experimental Data". *Fluid Mechanics,* ***656***, AUG, pp. 5–28.

[23] Kevin K. Chen, Jonathan H. Tu, C. W. R., 2012. "Variants of Dynamic Mode Decomposition: Boundary Conditions, Koopman, and Fourier Analyses". *Nonlinear Science,* ***22***(6), APR, pp. 887–915.

[24] Guckenheimer, J., and Holmes, P., 1986. *Nonlinear Oscillations, Dynamical Systems, and Bifurcations of Vector Fields*. Springer-Verlag.

[25] Lekien, F., Shadden, S. C., and Marsden, J. E., 2007. "Lagrangian coherent structures in *n*-dimensional systems". *J. Math. Phys.,* ***48***, p. 065404.

[26] Haller, G., 2000. "Finding finite-time invariant manifolds in two-dimensional velocity fields". *Chaos,* ***10***(1), pp. 99–108.

[27] Haller, G., 2001. "Distinguished material surfaces and coherent structures in three-dimensional fluid flows". *Physica D,* ***149***, pp. 248–277.

[28] Haller, G., 2002. "Lagrangian coherent structures from approximate velocity data". *Phys. Fluids,* ***14***(6), pp. 1851–1861.

[29] Shadden, S. C., Lekien, F., and Marsden, J. E., 2005. "Definition and properties of Lagrangian coherent structures from finite-time Lyapunov exponents in two-dimensional aperiodic flows". *Physica D,* ***212***, pp. 271–304.

[30] Branicki, M., and Wiggins, S., 2010. "Finite-time Lagrangian transport analysis: Stable and unstable manifolds of hyperbolic trajectories and finite-time Lyapunov exponents". *Nonlinear Proc. Geoph.,* ***17***, pp. 1–36.

[31] Tang, W., Chan, P. W., and Haller, G., 2010. "Accurate extraction of lagrangian coherent structures over finite domains with application to flight data analysis over hong kong international airport". *Chaos,* ***20***, p. 017502.

[32] Eldredge, J. D., and Chong, K., 2010. "Fluid transport and coherent structures of translating and flapping wings". *Chaos,* ***20***, p. 017509.

[33] Lukens, S., Yang, X., and Fauci, L., 2010. "Using lagrangian coherent structures to analyze fluid mixing by cilia". *Chaos,* ***20***, p. 017511.

[34] Haller, G., 2011. "A variational theory of hyperbolic lagrangian coherent structures". *Physica D,* ***240***, pp. 574–598.

[35] Agui, J. C., and Jimenez, J., 1987. "On the performance of particle tracking". *Journal of Fluid Mechanics,* ***185***, pp. 447–468.

[36] Marchioli, C., Armenio, V., and Soldati, A., 2007. "Simple and accurate scheme for fluid velocity interpolation for eulerianlagrangian computation of dispersed flows in 3d curvilinear grids". *Computers & Fluids,* ***36***, pp. 1187–1198.

[37] Fuselier, E. J., and Wright, G. B., 2009. "Stability and error estimates for vector field interpolation and decomposition on the sphere with rbfs". *SIAM J. Numer. Anal.,* ***47***, pp. 3213–3239.